Image Correlation Spectroscopy. II. Optimization for Ultrasensitive Detection of Preexisting Platelet-Derived Growth Factor-β Receptor Oligomers on Intact Cells

Paul W. Wiseman and Nils O. Petersen

Department of Chemistry, The University of Western Ontario, London, Ontario N6A 5B7, Canada

ABSTRACT   Previously we introduced image correlation spectroscopy (ICS) as an imaging analog of fluorescence correlation spectroscopy (FCS). Implementation of ICS with image collection via a standard fluorescence confocal microscope and computer-based autocorrelation analysis was shown to facilitate measurements of absolute number densities and determination of changes in aggregation state for fluorescently labeled macromolecules. In the present work we illustrate how to use ICS to quantify the aggregation state of immunolabeled plasma membrane receptors in an intact cellular milieu, taking into account background fluorescence. We introduce methods that enable us to completely remove white noise contributions from autocorrelation measurements for individual images and illustrate how to perform background corrections for autofluorescence and nonspecific fluorescence on cell population means obtained via ICS. The utilization of photon counting confocal imaging with ICS analysis in combination with the background correction techniques outlined enabled us to achieve very low detection limits with standard immunolabeling methods on normal, nontransformed human fibroblasts (AG1523) expressing relatively low numbers of platelet-derived growth factor-β (PDGF-β) receptors. Specifically, we determined that the PDGF-β receptors were preaggregated as tetramers on average with a mean surface density of 2.3 clusters μm^{-2} after immunolabeling at 4°C. These measurements, which show preclustering of PDGF-β receptors on the surface of normal human fibroblasts, contradict a fundamental assumption of the ligand-induced dimerization model for signal transduction and provide support for an alternative model that posits signal transduction from within preexisting receptor aggregates.

INTRODUCTION

Aggregation of macromolecules within the plasma membrane is believed to play a fundamental role in the regulation of various cellular activities, including the immune response and signal transduction (Metzger, 1992; Ullrich and Schlessinger, 1990). The is ligand-induced dimerization model is widely accepted and is invoked to explain the molecular mechanism of activation and signaling for many cell surface receptors, including the receptor tyrosine kinases (Lemmon and Schlessinger, 1994; Heldin, 1995). It posits that the signaling ligand binds to the extracellular domain of dispersed monomeric receptors in the plasma membrane, inducing the receptor subunits to dimerize. The dimerization event is hypothesized to be integral to activation of the receptor and subsequent transduction of the signal inside the cell. However, some researchers have questioned the experimental evidence supporting this model, as many experiments have involved detergent-solubilized receptors or reconstituted receptors in lipid bilayers. They have provided data that support alternative models involving signal transduction via conformational or rota-

tional changes after binding of the ligand to monomeric or preaggregated receptors (Carraway and Cerione, 1991, 1993; Gadella and Jovin, 1995). Considering the perceived ubiquity of macromolecular oligomerization as a biological control mechanism and the unresolved questions of its mechanistic role in signal transduction, it is essential to perform experiments that can directly assess the aggregation state of receptors on living or minimally perturbed intact cells. To achieve this goal, it is imperative to develop and implement new experimental techniques that allow complete characterization of oligomerization phenomena in such systems.

A variety of experimental techniques have been employed to study receptor clustering. Electron microscopy (EM) has provided high-resolution microscopic evidence of protein clustering within the plasma membrane (Van Belzen et al., 1988). However, as has been noted previously, EM is limited by difficulties with temporal resolution and potentially by artefacts introduced by harsh sample preparation techniques (Petersen et al., 1993; Huang and Thompson, 1996). Moreover, cell viability is compromised under nonphysiological preparation conditions, so measurements cannot be performed on living cells.

Fluorescence microscopy has been utilized to study macromolecular clustering in both artificial and intact cellular membranes. Early studies provided qualitative evidence of surface reorganization and clustering of receptors after the addition of ligand (Schlessinger et al., 1978; Haigler et al., 1978). The resolution limit inherent in such optical microscopy techniques precluded quantitative characterization of the oligomerization. More recently, fluorescence resonance

energy transfer (FRET) techniques have provided strong evidence of spatial colocalization of receptor macromolecules on the surface of living cells (Carraway and Cerione, 1991, 1993; Kubitscheck et al., 1991, 1993; Young et al., 1994; Gadella and Jovin, 1995). However, FRET does not yield information about the actual size of the aggregates. Fluorescence video imaging microscopy techniques have been successfully used to track the motions of receptor aggregates and simultaneously quantify the distribution of cluster size (Ghosh and Webb, 1994; Morrison et al., 1994). These methods are advantageous in that they provide complete information about the aggregation state in combination with a measurement of receptor motional dynamics. However, they are computationally intensive and require specialized labeling methods to yield sufficient fluorophore for imaging purposes.

There is a general class of fluorescence microscopy techniques collectively referred to as fluorescence correlation spectroscopy (FCS) that are uniquely suited for measurements of macromolecular aggregation (reviewed in Thompson, 1991). FCS methods are all characterized by autocorrelation analysis of fluorescence intensity fluctuations measured from a small observation volume (or area) that reflect the underlying temporal and/or spatial fluctuations in concentration of the fluorophore. One of the key advantages of the FCS method is that the measured autocorrelation function reflects and is sensitive to changes in the aggregation state of the fluorophore (Palmer and Thompson, 1989; Thompson, 1991; Meyer and Schindler, 1988; Petersen, 1986; Petersen et al., 1993). Recently, the availability of FCS methods has increased with the introduction of implementation on confocal laser scanning microscopes (CLSMs) (Petersen et al., 1993; Koppel et al., 1994) and variations involving total internal reflection illumination and imaging with charge-coupled device (CCD) detectors (Wang and Axelrod, 1994; Huang and Thompson, 1996).

In our earlier work we introduced image correlation spectroscopy (ICS) as a novel extension of the earlier scanning FCS (s-FCS) technique to the imaging regime (Petersen et al., 1993). The previous paper dealt with the background theory of ICS and technical details of performing ICS with a CLSM and gave some preliminary results on application of the method to detection of changes in the receptor aggregation state on intact cells. In the current work, we describe how to push the limits of detection of ICS so as to quantitatively measure the aggregation state of receptors on the surface of intact cells in culture. In particular, we provide details of how to improve detection and linearity by using digital photon counting and describe ways of minimizing and removing background, which is a problem inherent to fluorescence measurements on cellular systems. Implementation of these technical improvements is then demonstrated for ultrasensitive detection and characterization of PDGF-β receptor distribution on intact human dermal fibroblasts.

MATERIALS AND METHODS

Antibodies

The primary antibody, IgG PDGFR-B2, was purchased from the Sigma Chemical Company and had a total protein concentration of 21.6 mg/ml and an IgG concentration of 0.6 mg/ml (catalog no. P 7679; St. Louis, MO). The primary antibody was a mouse monoclonal IgG that binds specifically to the extracellular portion of human and porcine PDGF-β receptor but does not bind to PDGF-α receptors (Rönnstrand et al., 1988). The antibody induces clustering and a certain degree of down-regulation of the PDGF-β receptors at 37°C, but it does not have a mitogenic effect, nor does it block the binding of PDGF-BB to its receptors. The antibody will precipitate the receptors from a cell-free suspension. The primary antibody was used at various dilutions for labeling of the PDGF-β receptors.

A tetramethylrhodamine isothiocyanate-labeled goat anti-mouse polyclonal antibody specific for the Fab portion of mouse IgG was used as the secondary antibody for indirect immunofluorescence labeling of the PDGF-β receptors (catalog no. T 6528; Sigma). The TRITC-labeled IgG had a stock concentration of 5.8 mg/ml and was diluted by a factor of 1:32 with phosphate-buffered saline (PBS) for the labeling of all samples.

Cell culture

Human foreskin fibroblasts (AG1523) were purchased from the NIA Aging Cell Culture Repository, Coriell Institute for Medical Research (Camden, NJ). The cells are classified as apparently normal nonfetal tissue, fibroblast-like, normal diploid human male. The fibroblasts were maintained in a humidified incubator at 5% CO_2 atmosphere and cultured in Eagle's minimum essential medium (MEM) (with Earle's salts, without L-glutamine) (Gibco Laboratories Life Technologies, Grand Island, NY), supplemented with 10% fetal bovine serum (Gibco), 292 mg/liter L-glutamine (Sigma), 50 IU/ml penicillin (Gibco), and 50 μg/ml streptomycin (Gibco). Cells were plated onto 18-mm glass coverslips in 35 $\times$ 10 mm tissue culture flasks (Falcon; Becton Dickinson Labware and Co., Lincoln Park, NJ) containing MEM growth medium. The fibroblasts were cultured for 2 days before being used in experiments. Cells were switched to serum-free growth conditions on the second day and raised in serum-free medium for 24 h before experimental labeling. MCDB 104 medium (BioFluids, Rockville, MD) supplemented with 1 mg/ml bovine serum albumin was used to provide serum-free growth conditions.

Cell samples were labeled on ice (4°C) for 30 min with primary antibody at the following concentrations: 300, 120, 30, 6, or 0 μg/ml. After incubation with the primary label, the samples were rinsed extensively with cold PBS. Subsequently, samples were labeled with 181 μg/ml TRITC-conjugated secondary antibody for 30 min at 4°C. Samples were rinsed with cold PBS and then fixed with 4% (w/v) paraformaldehyde in PBS (pH 7.4) for 15 min. After fixation, the cells were rinsed with PBS and mounted on slides for viewing under the microscope. Two types of control samples were prepared along with the regular cell samples: primary antibody control (cells labeled with 120 μg/ml primary IgG and no secondary antibody) and secondary antibody control (cells labeled with 181 μg/ml secondary antibody and no primary antibody).

Confocal microscopy

A Biorad MRC600 CLSM (Biorad Microscience, Hertfordshire, England) with a 60$\times$ oil immersion objective lens (numerical aperture 1.4) was utilized for all measurements. Confocal scanning illumination was provided by a 25-mW argon ion laser, and the confocal pinhole was set to position 8 on the instrument's Vernier scale (corresponding to a confocal pinhole of diameter of 4.2 mm) (see Petersen et al., 1993). The GHS filter block for rhodamine imaging was inserted into the scan box of the instrument (excitation 514 nm, barrier filter 550 nm). All samples were imaged using the photon counting collection mode on the MRC 600 calibrated (via black level control) to ensure that at least one quantum event was detected per pixel per scan. Each image was collected as an accumulation of 25

individual scans in photon counting mode. All images to be used for subsequent ICS analysis were 512 by 512 pixels in size and were collected at a "zoom factor" of 10, which corresponded to a pixel dimension of 0.0318 μm in both the x and y directions. For each sample, at least 40 different cells were sampled, and the images were submitted for autocorrelation analysis. A "white noise" background image was obtained periodically every 5–10 min by initiating image acquisition with the light path to the sample blocked.

ICS analysis

The ICS analysis was conducted on the CLSM images obtained from each of the biological samples in the primary IgG concentration series as well as from the control specimens. For each sample, a series of S images ($S \approx 40$) and a corresponding series of periodically sampled white noise images were collected:

Specimen#

$$
\begin{aligned}
&\rightarrow \quad \text{image}_j \qquad \text{where } j = 1, 2, \ldots, S \\
&\rightarrow \quad \text{wn image}_j, \quad \text{where } j' = 1, 2, \ldots, T
\end{aligned} \quad T < S \quad (1)
$$

For each specimen, its corresponding series of S images collected from individual cells is a sampling of the underlying cell population.

Image correlation analysis was conducted for all of the images with a VAX 6340 mainframe computer at the Computing and Communications Services of the University of Western Ontario (London, ON, Canada). The ICS analysis involved calculating a discrete or raw autocorrelation function ($r(\xi, \eta)_j$) from each image, following procedures outlined in our earlier work (Petersen et al., 1993). A Gaussian function was fit to each raw autocorrelation function, using a three-parameter nonlinear least-squares fitting procedure:

$$
r(\xi, \eta)_j = \mathbf{g(0, 0)}_j \exp\left\{\frac{\xi^2 + \eta^2}{\omega_j^2}\right\} + \mathbf{g_{oj}} \quad (2)
$$

where the fitting parameters are printed in bold (Petersen et al., 1993). For each image j, a zero lags autocorrelation function amplitude (the $g(0, 0)_j$ value from the best fit function), best fit beam radius (ω_j), baseline offset fit parameter (g_{oj}), and the average image pixel intensity ($\langle i \rangle_j$) were obtained and output in ASCII files. Corresponding average pixel intensities were calculated for each white noise image ($\langle i_{wn} \rangle_{j'}$). The data and parameters obtained from ICS analysis of the images are summarized below:

$$
\begin{aligned}
\text{image}_j &\quad \rightarrow \quad \langle i \rangle_j, \quad r(\xi, \eta)_j \rightarrow g(0, 0)_j, \omega_j, g_{oj} \\
\text{wn image}_{j'} &\quad \rightarrow \quad \langle i_{wn} \rangle_{j'}
\end{aligned} \quad (3)
$$

White noise background correction

The zero lags autocorrelation function amplitude values and average intensities for each image were corrected for white noise background by using the average intensity from the appropriate white noise background image as outlined below:

$$
g(0, 0)_{cj} = \frac{g(0, 0)_j \langle i \rangle_j^2}{\{\langle i \rangle_j - \langle i_{wn} \rangle_{j'}\}^2}
$$
$$
\langle i \rangle_{cj} = \langle i \rangle_j - \langle i_{wn} \rangle_{j'} \quad (4)
$$

where the subscript c indicates parameters corrected for white noise background. Images collected from all cell samples, including the primary and secondary antibody controls, were corrected in this manner, and the white noise background corrected zero lags amplitudes and average intensity values were used for all subsequent calculations.

Cell population means

Average parameters for each sample and control cell population were calculated using the white noise background corrected data; however, to simplify the notation, the subscript c is dropped in the following equations. Furthermore, uppercase type is used to symbolize an average value calculated from the complete cell population (i.e., from all images collected from a specimen), and lowercase type is reserved for parameters derived from an individual image (i.e., from a single cell). For each sample, the (population) mean number of independent fluorescent entities per beam area (the occupation number) was calculated from the reciprocals of the individual $g(0, 0)_j$ values:

$$
\langle N \rangle = \frac{1}{S} \sum_{j=1}^{S} n_j \quad \text{where } n_j = g(0, 0)_j^{-1} \quad (5)
$$

Likewise, the population mean intensity was calculated as follows:

$$
\langle I \rangle = \frac{1}{S} \sum_{j=1}^{S} \langle i \rangle_j \quad (6)
$$

and a parameter called the degree of aggregation (DA) was obtained as a ratio of population means:

$$
\langle DA \rangle = \frac{\langle I \rangle}{\langle N \rangle} \quad (7)
$$

Background correction of cell population means

The cell population means for the highest concentration sample (representing saturation level binding of the primary IgG) were corrected for background fluorescence by utilizing the cell population means for the secondary antibody control. Similarly, the population means of the secondary antibody control sample were corrected for autofluorescence background by using the cell population averages determined for the primary antibody control sample. These two fluorescence background corrections provided estimates of the magnitudes of the cell population parameters arising from specifically (s) bound fluorophore as well as nonspecifically (ns) bound fluorophore and were performed as follows:

$$
\langle N_s \rangle = \left\{ \frac{\langle N \rangle_h^{-1} \langle I \rangle_h^2 - \langle N \rangle_{2°}^{-1} \langle I \rangle_{2°}^2}{[\langle I \rangle_h - \langle I \rangle_{2°}]^2} \right\}^{+1} \quad (8)
$$

$$
\langle I_s \rangle = \langle I \rangle_h - \langle I \rangle_{2°} \quad (9)
$$

$$
\langle N_{ns} \rangle = \left\{ \frac{\langle N \rangle_{2°}^{-1} \langle I \rangle_{2°}^2 - \langle N \rangle_{1°}^{-1} \langle I \rangle_{1°}^2}{[\langle I \rangle_{2°} - \langle I \rangle_{1°}]^2} \right\}^{-1} \quad (10)
$$

$$
\langle I_{ns} \rangle = \langle I \rangle_{2°} - \langle I \rangle_{1°} \quad (11)
$$

The subscripts 2° and 1° indicate population mean parameters for the secondary and primary antibody control samples, respectively, and the subscript h indicates data obtained for the highest concentration sample (300 μg/ml 1° IgG). An explanation of the derivation of these equations and assumptions involved will be deferred until the Theory section. These data were then substituted into Eq. 7 and used to calculate the mean degree of aggregation of the specifically and nonspecifically bound fluorophore for the sampled populations.

All data analysis apart from the calculation of the raw autocorrelation function and nonlinear least-squares fitting was done using Sigma Plot for Windows version 2.0 (Jandel Scientific, San Rafael, CA). All plots were constructed using Sigma Plot for Windows version 2.0 or Stanford Graphics version 3.0 (Visual Numerics, Torrance, CA).

THEORY

The theoretical basis of ICS was introduced in our earlier work (Petersen et al., 1993). In the following, we recapitulate and reformulate some of the basic definitions to facilitate the introduction of concepts concerning background effects that are integral to the current work.

The seminal measurement of ICS is the determination of fluorescence intensity excited from a small area on the membrane of an immunolabeled cell. The observation area is defined by the diffraction-limited focal spot of the exciting laser beam, which is swept in raster fashion across the surface of the cell by the scanning mechanism of the CLSM. At each discrete step in the raster scan, fluorescence photons are collected by the optical system and detected, and the resulting counts are rendered into a two-dimensional array of pixel intensities that constitutes the CLSM image. For each pixel in the image, the fluorescence intensity fluctuation is defined as

$$\delta i(x, y) = i(x, y) - \langle i \rangle \qquad (12)$$

where $i(x, y)$ is the intensity (photon count) of pixel location x, y and $\langle i \rangle$ is the mean intensity of the image.

For an ideal system of noninteracting fluorescent particles in a system with no fluorescence background, the ratio of the mean square intensity fluctuation to the square of the mean intensity is equal to the reciprocal of the mean number of independent fluorescent particles per beam area ($\langle n \rangle$) and is referred to as the square relative intensity fluctuation:

$$\frac{\langle (\delta i)^2 \rangle}{\langle i \rangle^2} = \frac{1}{\langle n \rangle} \qquad (13)$$

For such an ideal system, it would be possible to calculate the mean occupation number by calculating the square relative fluctuation directly from the image intensity data. However, for real systems, such a direct calculation of $\langle n \rangle$ is impossible because of the combined effects of various sources of fluorescence background counts (both real and spurious).

Each pixel in the CLSM image has an integer intensity value (total photon count), which is the sum of separate contributions from counts due to fluorescence arising from specifically bound fluorophore (s), nonspecifically bound fluorophore (ns), autofluorescence background (a), and white noise counts mainly due to shot noise, dark current of the PMT, and scattered laser light in the scan box (wn):

$$i(x, y) = i_s(x, y) + i_{ns}(x, y) + i_a(x, y) + i_{wn}(x, y) \qquad (14)$$

It follows that the average intensity of an image can be broken down into terms representing the average contribution of each of these sources of intensity counts:

$$\langle i \rangle = \langle i_s \rangle + \langle i_{ns} \rangle + \langle i_a \rangle + \langle i_{wn} \rangle \qquad (15)$$

Likewise, by substituting Eqs. 14 and 15 into Eq. 12, it is easy to show that each fluorescence intensity fluctuation

magnitude is the sum of the fluctuations arising from the individual sources of photon counts:

$$\delta i(x, y) = \delta i_s(x, y) + \delta i_{ns}(x, y) + \delta i_a(x, y) + \delta i_{wn}(x, y) \qquad (16)$$

Thus the mean square intensity fluctuation for a particular image will be given by the following expression:

$$\langle (\delta i)^2 \rangle = \langle (\delta i_s + \delta i_{ns} + \delta i_a + \delta i_{wn})^2 \rangle \qquad (17)$$

which simplifies to

$$\langle (\delta i)^2 \rangle = \langle (\delta i_s)^2 \rangle + \langle (\delta i_{ns})^2 \rangle + \langle (\delta i_a)^2 \rangle + \langle (\delta i_{wn})^2 \rangle \qquad (18)$$

if we assume that the mean cross-fluctuation terms in the expansion of Eq. 17 go to zero. This assumption is valid if the individual sources of intensity counts are not spatially correlated across the image. This is quite reasonable, as the cross terms would be nonzero only in an unlikely situation where the sources of background fluorescence were always spatially coincident with the specifically bound fluorophore.

In ICS analysis, the image intensity data are used to calculate a normalized fluorescence fluctuation autocorrelation function. This normalized intensity fluctuation autocorrelation function is defined as follows:

$$r(\xi, \eta) = \frac{\langle \delta i(x, y) \delta i(x + \xi, y + \eta) \rangle}{\langle i \rangle^2} \qquad (19)$$

where the angle brackets indicate spatial averaging. This is a discrete function of two independent spatial lag variables, and we refer to this function as the raw or discrete autocorrelation function. The zero lags amplitude of the autocorrelation function is the square relative intensity fluctuation:

$$r(0, 0) = \frac{\langle (\delta i)^2 \rangle}{\langle i \rangle^2} = \frac{\langle (\delta i_s)^2 \rangle + \langle (\delta i_{ns})^2 \rangle + \langle (\delta i_a)^2 \rangle + \langle (\delta i_{wn})^2 \rangle}{[\langle i_s \rangle + \langle i_{ns} \rangle + \langle i_a \rangle + \langle i_{wn} \rangle]^2} \qquad (20)$$

However, in experimental practice, the zero lags amplitude of the autocorrelation function is not directly calculated because of the significant white noise component. The ICS analysis outputs a fit parameter referred to as the $g(0, 0)$ value, which is determined via nonlinear least-squares fitting of a Gaussian function to the raw autocorrelation function, as explained in Materials and Methods (see Eq. 2). The $g(0, 0)$ value is the autocorrelation function amplitude above background level in the limit as the spatial lag variables approach zero:

$$g(0, 0) = \lim_{\xi, \eta \leftarrow 0} r(\xi, \eta) - g_o \qquad (21)$$

As the $r(0, 0)$ value receives zero weight in the fitting procedure, this method effectively removes the contribution of the mean square fluctuation term due to white noise from the $g(0, 0)$ value (i.e., $\langle (\delta i_{wn})^2 \rangle \rightarrow 0$ by virtue of the fitting procedure). However, the autocorrelation function (and hence $g(0, 0)$) is still normalized by the average image

intensity, which includes a white noise component:

$$g(0, 0) = \frac{\langle(\delta i)^2\rangle}{\langle i\rangle^2} = \frac{\langle(\delta i_s)^2\rangle + \langle(\delta i_{ns})^2\rangle + \langle(\delta i_a)^2\rangle}{[\langle i_s\rangle + \langle i_{ns}\rangle + \langle i_a\rangle + \langle i_{wn}\rangle]^2} \quad (22)$$

The white noise contribution in the denominator of Eq. 22 may be corrected for if we have an estimate of the magnitude of the mean intensity due to white noise counts. As the mean intensity terms are additive (Eq. 15), the average intensity for an image may be corrected for the white noise component by subtracting the average intensity of its paired background image:

$$\langle i\rangle_c = \langle i\rangle - \langle i_{wn}\rangle = \langle i_s\rangle + \langle i_{ns}\rangle + \langle i_a\rangle \quad (23)$$

Correction of the $g(0, 0)$ value for the white noise component simply involves normalization of the mean square fluctuation terms (numerator of Eq. 22) by the white noise corrected mean intensity (Eq. 23). The mean square fluctuation terms may be isolated simply by multiplying the $g(0, 0)$ value by the normalizing factor, $\langle i\rangle^2$ (see Eq. 22). Thus isolation of the mean square fluctuation terms in the numerator followed by renormalization with the white noise corrected mean intensity eliminates the contribution of the white noise component from the denominator of Eq. 22:

$$g(0, 0)_c = \frac{g(0, 0)\langle i\rangle^2}{[\langle i\rangle - \langle i_{wn}\rangle]^2} = \frac{\langle(\delta i_s)^2\rangle + \langle(\delta i_{ns})^2\rangle + \langle(\delta i_a)^2\rangle}{[\langle i_s\rangle + \langle i_{ns}\rangle + \langle i_a\rangle]^2} \quad (24)$$

Equations 23 and 24 show the componentwise contributions for white noise corrected sample image data. Similar equations apply for the secondary and primary antibody control image data that have been corrected for white noise, but with contributions from the nonspecific and autofluorescence terms to the former and only the autofluorescence terms to the latter. Background correction methods for white spectrum background noise have been previously reported for FCS studies of ligand binding and kinetics (Icenogle and Elson, 1983; Thompson and Axelrod, 1983).

In an analogous manner, it would be possible to correct for the contributions of the various background terms arising from nonspecific fluorescence and autofluorescence if we had an estimate of the magnitude of each background component. Unfortunately, we do not have a way to determine the contributions of background within each image. However, we may obtain estimates of the mean magnitude of the background components for a cell population from measurements on control samples and subsequently perform background corrections on the cell population means of the regular samples.

The primary antibody control sample (1°) is labeled only with the primary monoclonal IgG, and measurements on this control allow cell population averages for autofluorescence background to be estimated:

$$\langle I\rangle_{1°} = \langle I_a\rangle \quad (25)$$

$$\langle N\rangle_{1°} = \frac{\langle I_a\rangle^2}{\langle(\delta I_a)^2\rangle} \quad (26)$$

$$\langle(\delta I_a)^2\rangle = [\langle N\rangle_{1°}]^{-1}\langle I_a\rangle^2 \quad (27)$$

The secondary antibody control sample (2°) is labeled solely with the fluorophore-conjugated secondary IgG. The cell population means for this control contain components arising from both nonspecific fluorescence and cellular autofluorescence:

$$\langle I\rangle_{2°} = \langle I_{ns}\rangle + \langle I_a\rangle \quad (28)$$

$$\langle N\rangle_{2°} = \frac{\langle I\rangle_{2°}^2}{\langle(\delta I)^2\rangle_{2°}} = \frac{[\langle I_{ns}\rangle + \langle I_a\rangle]^2}{\langle(\delta I_{ns})^2\rangle + \langle(\delta I_a)^2\rangle} \quad (29)$$

$$\langle(\delta I)^2\rangle_{2°} = [\langle N\rangle_{2°}]^{-1}\langle I\rangle_{2°}^2 = \langle(\delta I_{ns})^2\rangle + \langle(\delta I_a)^2\rangle \quad (30)$$

By using the cell population averages for the 1° IgG control (Eqs. 25 and 27), it is possible to correct the 2° IgG control data and calculate estimates of the magnitudes of the cell population means for nonspecific fluorescence:

$$\langle I_{ns}\rangle = \langle I\rangle_{2°} - \langle I\rangle_{1°} \quad (31)$$

$$\langle(\delta I_{ns})^2\rangle = [\langle N\rangle_{2°}]^{-1}\langle I\rangle_{2°}^2 - [\langle N\rangle_{1°}]^{-1}\langle I\rangle_{1°}^2$$

$$= \langle(\delta I)^2\rangle_{2°} - \langle(\delta I)^2\rangle_{1°} \quad (32)$$

$$\langle N_{ns}\rangle = \frac{\langle I_{ns}\rangle^2}{\langle(\delta I_{ns})^2\rangle} = \frac{[\langle I\rangle_{2°} - \langle I\rangle_{1°}]^2}{\langle(\delta I)^2\rangle_{2°} - \langle(\delta I)^2\rangle_{1°}} \quad (33)$$

The cell population means for the noncontrol samples will contain terms that derive from specific fluorescence, nonspecific fluorescence, and autofluorescence:

$$\langle I\rangle = \langle I_s\rangle + \langle I_{ns}\rangle + \langle I_a\rangle \quad (34)$$

$$\langle N\rangle = \frac{\langle I\rangle^2}{\langle(\delta I)^2\rangle} = \frac{[\langle I_s\rangle + \langle I_{ns}\rangle + \langle I_a\rangle]^2}{\langle(\delta I_s)^2\rangle + \langle(\delta I_{ns})^2\rangle + \langle(\delta I_a)^2\rangle} \quad (35)$$

$$\langle(\delta I)^2\rangle = [\langle N\rangle]^{-1}\langle I\rangle^2 = \langle(\delta I_s)^2\rangle + \langle(\delta I_{ns})^2\rangle + \langle(\delta I_a)^2\rangle \quad (36)$$

Likewise, it is possible to correct the population averages of the regular samples to obtain estimates for the specific fluorescence terms. This correction is made using the population mean parameters determined for the 2° IgG control (Eqs. 28 and 30):

$$\langle I_s\rangle = \langle I\rangle - \langle I\rangle_{2°} \quad (37)$$

$$\langle(\delta I_s)^2\rangle = [\langle N\rangle]^{-1}\langle I\rangle^2 - [\langle N\rangle_{2°}]^{-1}\langle I\rangle_{2°}^2 = \langle(\delta I)^2\rangle - \langle(\delta I)^2\rangle_{2°} \quad (38)$$

$$\langle N_s\rangle = \frac{\langle I_s\rangle^2}{\langle(\delta I)_s^2\rangle} = \frac{[\langle I\rangle - \langle I\rangle_{2°}]^2}{\langle(\delta I)^2\rangle - \langle(\delta I)^2\rangle_{2°}} \quad (39)$$

As for the correction of white noise background, the implicit assumption for the background correction of the cell population means is that the individual mean square fluctuation terms and the average intensity terms are addi-

tive. A similar background correction procedure was employed in an earlier work (St-Pierre and Petersen, 1992).

RESULTS AND DISCUSSION

For ICS measurements of receptor distributions on intact cells, it is imperative to use pulse counting for PMT detection. Utilization of discrete photon counting eliminates multiplicative noise inherent to analog detection, which can augment the uncertainty due to fundamental quantal photon noise by 15–30% (Pawley, 1995). For quantitative imaging of immunolabeled receptors on the surface of cells, photon counting is essential because of the relatively small numbers of receptors that are expressed in biological systems and the low photon collection efficiency of commercial confocal microscopes. Images collected by operating a CLSM in pulse counting mode will have an uncertainty in pixel intensity governed solely by Poisson statistics; moreover, the intensities will scale linearly across the image as long as the maximum counting rate of the detection system is not exceeded. The ICS measurements of the PDGF-β receptors on AG1523 fibroblasts were carried out on CLSM images that had been collected using photon counting detection. The number of photons per scan for the brightest pixels was about half the maximum counting rate for the commercial instrument used in this study, thus ensuring that the assumption of linearity is valid.

In Fig. 1 we present an overview of CLSM images of immunolabeled PDGF-β receptors on AG1523 fibroblasts collected in this ICS experiment. Fig. 1 *A* displays a low zoom image of an AG1523 fibroblast in which the distribution of immunolabeled PDGF-β receptors across the surface of the cell may be seen. The arrow in Fig. 1 *A* marks areas of higher autofluorescence background in the perinuclear region. The rectangle superimposed on the image outlines an area from which a "high zoom" image was sampled for ICS analysis. This region is rectangular because the MRC600 CLSM would scan an area comprising 768 $\times$ 512 pixels, although the actual high zoom image rendered on the monitor and saved was a 512 $\times$ 512 pixels square image. The high zoom images used for ICS analysis were always sampled from such peripheral membrane areas on the cells so as to avoid the greater autofluorescence background that characterized the regions in the vicinity of the nucleus. Care was exercised during high zoom image acquisition to ensure that only regions of the cell surface were imaged so as to avoid edge and boundary effects that would perturb the calculated autocorrelation function. Fig. 1 *B* shows a typical high zoom image that was collected in this experiment. The surface distribution of immunolabeled PDGF-β receptors is more readily appreciated in this higher resolution image, and a wide range in the fluorescence intensity as a function of position is evident from visual inspection. The high zoom CLSM image shown in Fig. 1 *B* and its paired background image represent the starting point in the ICS analysis.
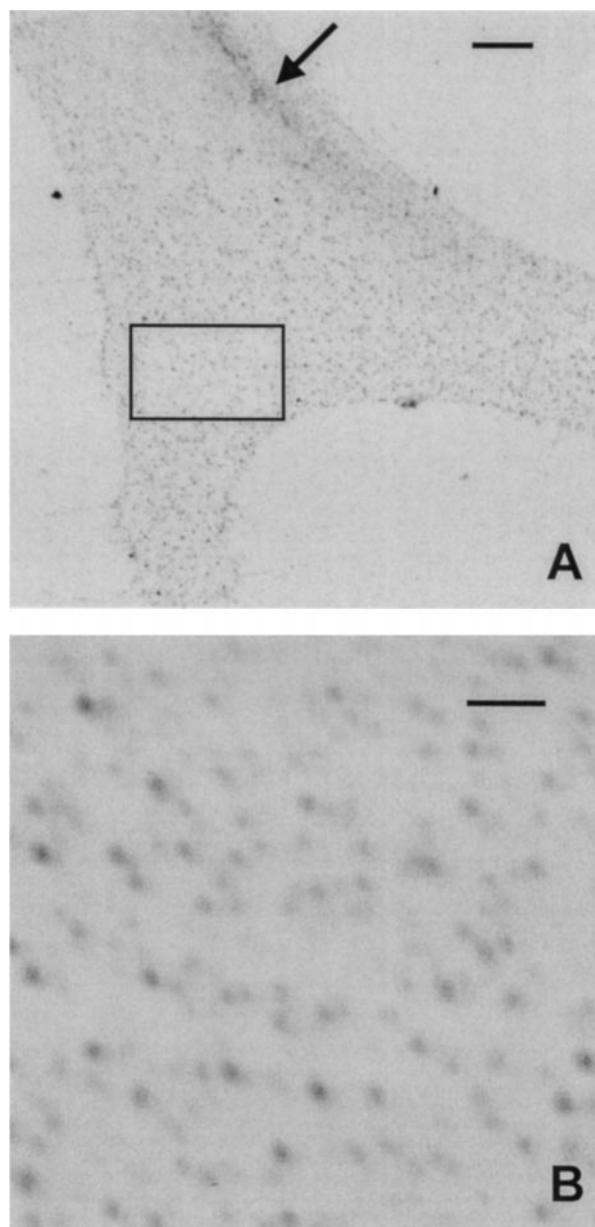

FIGURE 1   Confocal images of immunolabeled PDGF-β receptors on the surface of human AG1523 fibroblasts, collected using a Biorad MRC600 CLSM. (*A*) A low zoom (1.5$\times$) CLSM image of an AG1523 fibroblast, showing the surface distribution of indirectly immunolabeled PDGF-β receptors. The image was collected in photon-counting mode as an accumulation of 18 scans using rhodamine optics. The look-up table for this image was inverted to allow fainter objects to be more readily discerned (inverted grayscale white = 0; black = 255). The arrow points to brighter regions of autofluorescence in the perinuclear area. The rectangular box marks off an area from which a high zoom image has been sampled for ICS analysis. The scale bar represents 10 μm. (*B*) A high zoom (10$\times$) CLSM image of an area of plasma membrane sampled from an AG1523 fibroblast, showing the surface distribution of indirectly immunolabeled PDGF-β receptors at higher resolution. The image was collected in photon-counting mode as an accumulation of 25 scans, using rhodamine optics from the sample labeled with 120 μg/ml 1° IgG. The look-up table for this image was inverted to allow fainter fluorescence spots to be more readily discerned (inverted grayscale white = 0; black = 255). This image is a typical cell sampled image and was analyzed using ICS. The scale bar depicts a length of 2 μm.
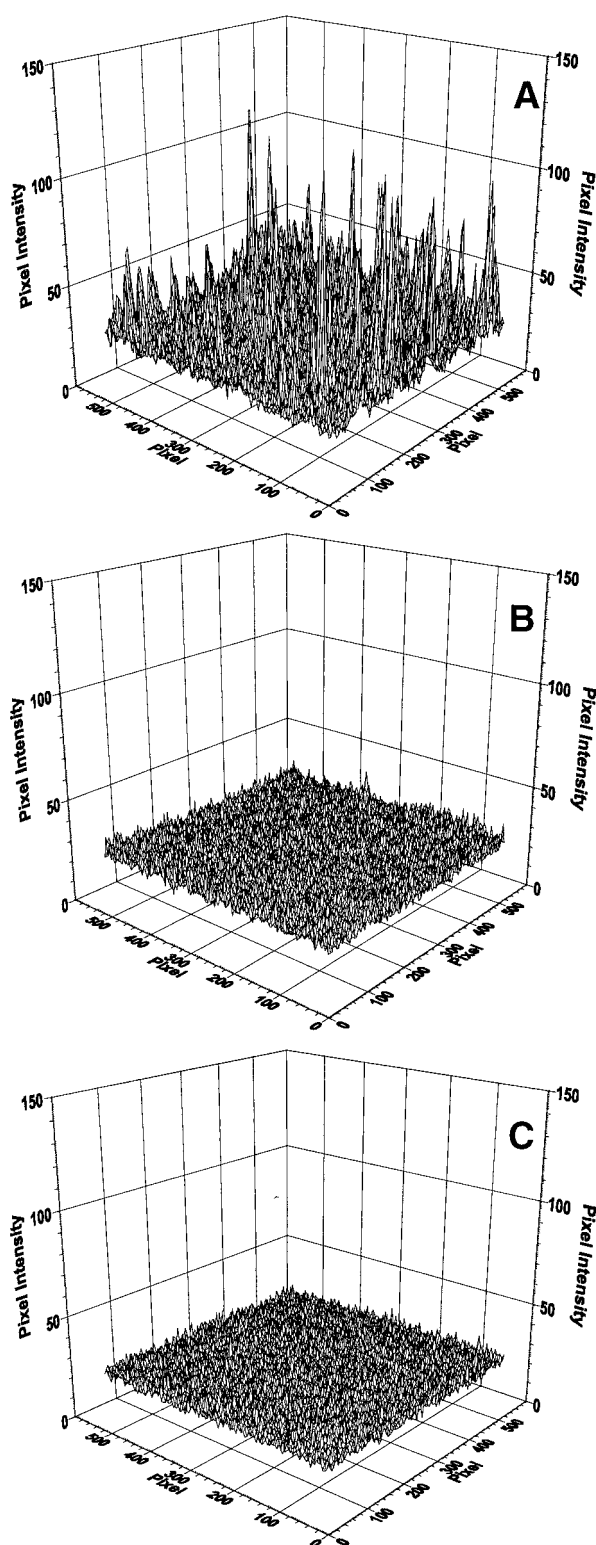
FIGURE 2   Plots of pixel intensity versus pixel number for high zoom sample image and its paired background image, along with a secondary antibody control image. (*A*) A plot of pixel intensity (photon count) versus image pixel location obtained from the high zoom sample image depicted in Fig. 1 *B*. (*B*) Analogous plot for a secondary antibody control image recorded in this experiment. (*C*) The corresponding plot of photon count versus pixel number for the paired background image obtained immediately after collection of the image shown in Fig. 1 *B*. The background image was sampled with the light path to the sample blocked, but with the

Fig. 2 depicts plots of the intensity as a function of pixel position for the sample image presented in Fig. 1 *B* (Fig. 2 *A*), for a secondary antibody control image (Fig. 2 *B*), and for the background image (Fig. 2 *C*), which was measured after collection of the high zoom sample image in Fig. 1 *B*. In Fig. 2 *A* the Gaussian peaks rising out of the background noise level represent a convolution of the integrating laser beam with fluorescent, spatially localized point sources. The secondary antibody control intensity plot shown in Fig. 2 *B* also exhibits peaks of Gaussian shape, but of reduced intensity as compared to those in Fig. 2 *A*. The levels of the background counts are of comparable magnitude for both images. The plot of intensity versus pixel position for the background image (Fig. 2 *C*) shows that this uniform background noise level corresponds mainly to spurious counts arising within the PMT.

Fig. 3 provides confirmation that the background image contains only white spectrum noise. Fig. 3 *A* displays the raw normalized intensity fluctuation autocorrelation function ($r(\xi, \eta)$) calculated from the sample image in Fig. 1 *B*, and Fig. 3 *B* shows the equivalent discrete autocorrelation function determined from the secondary antibody control image (Fig. 2 *B*). The Gaussian decay of the autocorrelation function, which mirrors that of the transverse intensity profile of the integrating and correlating laser beam, is readily apparent in both, as is the white noise delta function in the zero lags channel ($r(0, 0)$). The corresponding autocorrelation function for the background image (Fig. 2 *C*) is presented in Fig. 3 *C*. The solitary delta function in Fig. 3 *C* proves that the fluctuations in the uniform background level have a white noise spectrum (i.e., they are random and do not correlate at nonzero spatial lags).

Fig. 4 redisplays the normalized autocorrelation functions for the sample image (Fig. 4 *A*) and the secondary antibody control image (Fig. 4 *B*), but with the Gaussian function of best fit displayed in the near quadrant. The fit function only reflects the contributions from beam correlated fluctuations at nonzero spatial lags and is not influenced by the white noise present in the zero lags channel of the raw autocorrelation function. Fig. 4 illustrates that the $g(0, 0)$ determined from the best fit to the raw autocorrelation function does not include a white noise mean square fluctuation component (see Eq. 22 and compare Figs. 3 and 4).

However, the $g(0, 0)$ value is determined from the normalized autocorrelation function, and the normalization factor ($\langle i \rangle^2$) also includes a white noise component (see Theory). As the average intensity is a necessary normalization factor in all forms of FCS, earlier studies that employed FCS to measure ligand binding kinetics also discussed similar corrections for white noise (Icenogle and Elson, 1983; Thompson and Axelrod, 1983). In the present study, the

rest of the microscope settings the same as for its paired sample image. To facilitate easier three-dimensional representation and graphing, the intensities plotted in both figures were sampled at one-fourth resolution in both orthogonal linear dimensions from the original images.
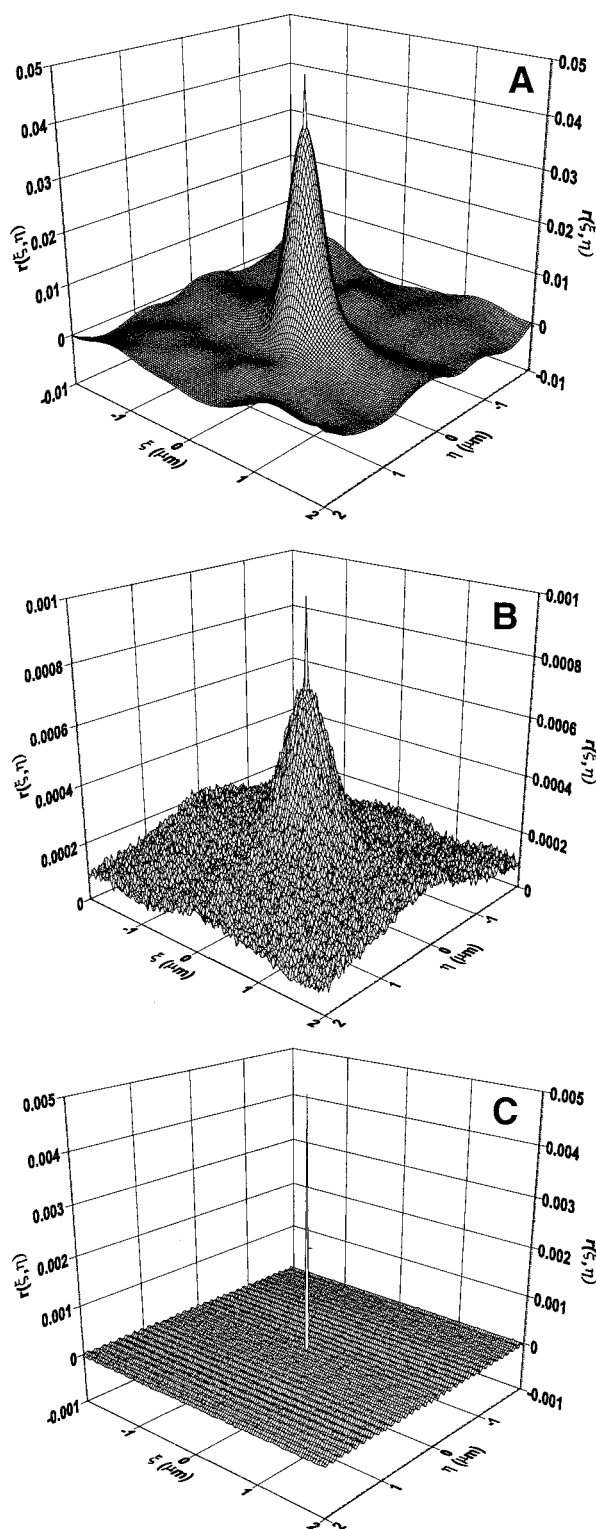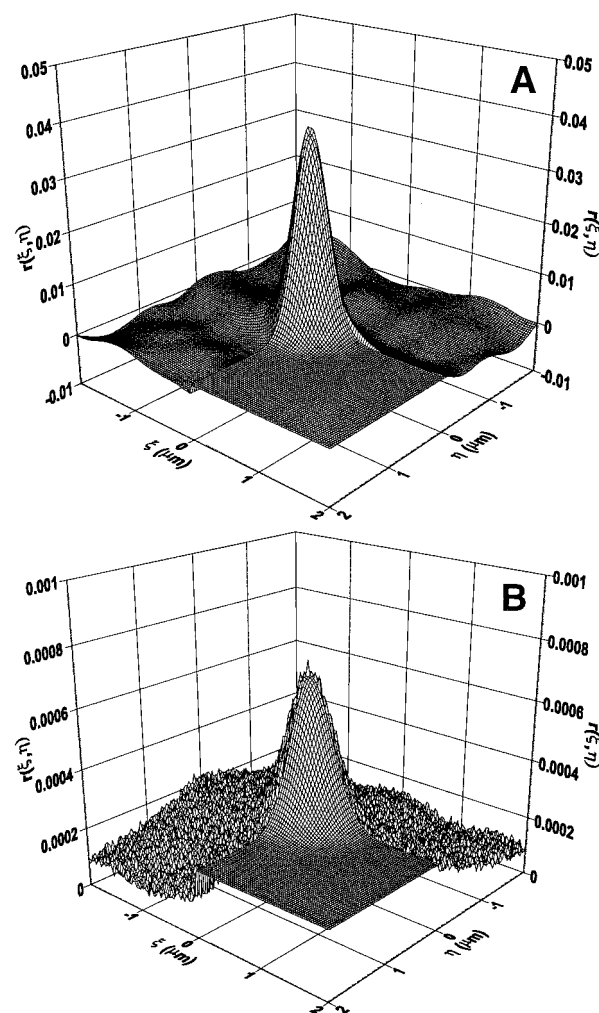
FIGURE 4   Autocorrelation functions with functions of best fit for high zoom sample image and the secondary antibody control image. (*A*) Plot of the discrete or raw autocorrelation function and Gaussian function of best fit as functions of spatial lags for the high zoom image from Fig. 1 *B*. (*B*) Corresponding autocorrelation function and Gaussian function of best fit for the secondary antibody control image that was intensity profiled in Fig. 2 *B*. Both autocorrelation plots depict the central 128 × 128 lag channels at full resolution. The fit function data are presented in the foreground (positive lags) quadrant, and the raw autocorrelation data are plotted in the other three quadrants for both plots.

immunolabeled biological samples have characteristically low levels of fluorescence signal, making it essential to correct the systematic errors arising from white noise contributions in the normalization factor. For the image presented in Fig. 1 *B*, the $g(0, 0)$ calculated directly without white noise correction (Eq. 22) is 0.0376, whereas the white

FIGURE 3   Autocorrelation functions for high zoom sample image and its paired background image, as well as for the secondary antibody control image. (*A*) Plot of the discrete or raw autocorrelation function as a function of spatial lags (pixel shifts) in the two orthogonal image dimensions, as calculated from the high zoom image presented in Fig. 1 *B*. (*B*) Plot of the corresponding raw autocorrelation function as a function of independent spatial lags, as calculated from the secondary antibody control image that was intensity profiled in Fig. 2 *B*. (*C*) Plot of the discrete or raw autocorrelation function as a function of independent spatial lags, as calculated

from the background image that was intensity profiled in Fig. 2 *C*. All three autocorrelation plots depict the central 128 × 128 lag channels at full resolution. Note that a truncated range of the autocorrelation amplitude axis was used in *B* to emphasize the Gaussian decay of the nonzero spatial lags data. Consequently, the full amplitude of the white noise peak in the zero lags channel of the autocorrelation function is not displayed ($r(0, 0) = 0.0069$).

noise corrected $g(0, 0)_c$ (Eq. 24) is 1.38. By performing background imaging concurrently with the sample imaging and performing the simple correction, we are able to completely remove the effects of white noise from the ICS results on an image-by-image basis.

An analogous correction can be made by subtracting the average background count from every pixel in an image before calculation of the normalized autocorrelation function (Wiseman, 1995). However, the postcorrelation correction method illustrated above is easy to implement within a spreadsheet program on a PC and reduces the number of calculations required for ICS analysis on the mainframe. Moreover, it is slightly more accurate, as it involves real arithmetic as opposed to an integer correction of the photon counts in the original image (Wiseman, 1995).

In this study, we averaged the $g(0, 0)_j^{-1}$ values to calculate cell population mean occupation numbers instead of averaging the individual $g(0, 0)_j$ values (Eq. 5). This approach was predicated on basic considerations of uncertainty in the determination of the individual $g(0, 0)_j$ values as compared to the uncertainty or distribution in the receptor occupation numbers observed for the cell populations. The uncertainty in the experimental data stems from two sources: instrumental uncertainty and biological variability. The former is a fundamental measurement uncertainty arising from quantal limits in the collection and detection of photons by the optics of the CLSM and from the stochastic nature of the ICS measurement. On the other hand, the biological variability arises from variations in the number of receptors expressed on the surface of different cells in the population. This uncertainty is characteristic of the system being studied but is not inherent to the actual ICS measurement. At the fundamental level of an ICS measurement, the biological variation will be manifested as differences in the number of receptors present on the membrane in the observation area defined by the focussed laser beam.

Instrumental uncertainties in ICS measurements

The $g(0, 0)$ value is an estimate of the true autocorrelation function amplitude above background as calculated from correlated fluctuations in the image. As can be seen in Eq. 21, the $g(0, 0)$ value is determined as the difference between two parameters from the function of best fit. The variance in a $g(0, 0)$ value will consequently be equal to the sum of the variances of the two terms in Eq. 21:

$$\sigma^2_{g(0, 0)} = \sigma^2_{r(0, 0)} + \sigma^2_{g_o} \qquad (40)$$

To provide an estimate of the uncertainty of the first term in Eq. 40, we considered the fundamental definition of the raw or discrete autocorrelation function evaluated at zero spatial lags ($r(0, 0)$; see Eq. 20). The amplitude is a function of the image intensities of the pixels composing the image. We assumed that the individual photon counts were governed by Poisson statistics, so that the standard deviation of each intensity was equal to the square root of the photon count for that pixel. Using this assumption and employing standard propagation of errors analysis, we derived the following equation for the variance in the zero lags amplitude value:

$$\sigma^2_{r(0,0)} = \frac{4}{N^2}\left\{\frac{\langle i\rangle\langle i^3\rangle - \langle i^2\rangle}{\langle i\rangle^5}\right\} \qquad (41)$$

where N^2 is the total number of pixels in a square image, and the angle brackets indicate averages calculated to yield the appropriate moments of the intensity variable. The zero lags amplitude includes a white noise component, which is indicated by the italic subscript $r(0, 0)$ in Eq. 41. However, the white noise fluctuations are spatially independent of the beam correlated fluorescence fluctuations. In this case the two variances are additive, and it is possible to subtract the variance in $r(0, 0)$ calculated via Eq. 41 for the white noise background image from that of the raw image to yield a rough estimate of the uncertainty in $r(0, 0)$ as determined via the fitting procedure:

$$\sigma^2_{r(0,0)} \approx \sigma^2_{r(0,0)} - \sigma^2_{r(0,0)\text{bgimage}} \qquad (42)$$

We used Eq. 41 to calculate the variance in $r(0, 0)$ for a number of images and their corresponding white noise background images and then employed Eq. 42 to provide an estimate of the uncertainty in $r(0, 0)$ independent of white noise. Table 1 summarizes the results of this calculation for a series of five images and their corresponding background image taken from the data set collected for the 120 μg/ml primary IgG sample. Table 1 shows that the relative uncertainty in the determination of $r(0, 0)$ ranges between 0.5 and 1% for these images. This was the typical range in the uncertainty of $r(0, 0)$ observed for images in this experiment.

In the absence of image artifacts such as edge effects, the uncertainty in determining the offset parameter g_o should reflect the uncertainty in defining this level against a background noise level of correlations at large spatial lags (i.e., spatial lags greater than the spatial extent of beam-correlated fluorescence fluctuations). This background arises because of the stochastic nature of the correlation measure-

TABLE 1 Uncertainty in the estimate of r(0, 0)

Image	$r(0, 0)$	$\sigma^2_{r(0, 0)}$	$\sigma^2_{\text{bg image*}}$	$\sigma^2_{r(0, 0)}$	$\sigma_{r(0, 0)}$	$\sigma_{r(0, 0)}/r(0, 0)$
1	1.46×10^{-2}	1.22×10^{-8}	3.2×10^{-9}	9.0×10^{-9}	9.5×10^{-5}	6.0×10^{-3}
2	1.84×10^{-2}	1.32×10^{-8}	3.2×10^{-9}	9.9×10^{-9}	1.0×10^{-4}	5.4×10^{-3}
3	7.69×10^{-3}	7.8×10^{-9}	3.2×10^{-9}	4.6×10^{-9}	6.8×10^{-5}	8.7×10^{-3}
4	8.57×10^{-3}	7.9×10^{-9}	3.2×10^{-9}	4.6×10^{-9}	6.8×10^{-5}	7.4×10^{-3}
5	6.04×10^{-3}	7.0×10^{-9}	3.2×10^{-9}	3.8×10^{-9}	6.1×10^{-5}	1.0×10^{-2}

*Note that the same white noise background image was used for this series of images.

ment and the practical limitation imposed by finite sampling (Koppel, 1974; Qian, 1990). The stochastic uncertainty is inversely proportional to the square root of the number of independent spatial intensity fluctuations that are sampled in the ICS measurement. In this experiment, the image area was 265 μm^2 and the beam area was 0.50 μm^2, which corresponds to 530 independent samples across an image. Thus the relative uncertainty in the determination of the amplitude of the correlation function above stochastic background correlations is

$$\frac{\sigma}{r(0,0)} = \frac{1}{\sqrt{530}} = 0.043 \qquad (43)$$

where σ is the standard deviation due to the stochastic effects.

We used Eq. 43 to determine the stochastic variance for each of the five images previously cited in Table 1. Addition of the variance in the determination of $r(0, 0)$ (Table 1) to that of the stochastic variance due to correlative background yields the overall variance for the determination of the $g(0, 0)$ value (Eq. 40). Table 2 summarizes these results for the five images and provides an indication of the overall uncertainty in the estimation of the $g(0, 0)$ values from images of PDGF-β receptors collected in this experiment. Table 2 demonstrates that the relative error in $g(0, 0)$ due to instrumental uncertainty is around 4.5% for this ICS experiment.

Qian points out that the signal-to-noise ratio (S/N) for FCS-type measurements will depend on the square root of the product of the number of fluorescent particles in the beam area and the number of fluctuations (data points) sampled when the mean photon count per particle is much greater than unity and when there are few particles in the beam area on average (Qian, 1990). As the S/N is the reciprocal of the relative error of $g(0, 0)$, it is possible to compare our determination of the instrumental uncertainty to that based on Qian's theoretical approach. In the experiments reported in this work, typically one PDGF-β receptor cluster was detected per beam area, and there were around 530 independent fluctuation areas sampled for each image. Using Qian's approach, we obtain a relative error of ~4.3% for these experiments, which compares favorably with our estimate.

Biological variability

To determine the spread in the data arising from cell-to-cell variations in receptor expression, we determined the cell population mean occupation number ($\langle N \rangle$; see Eq. 5), along with the variance and standard deviation for the cellular distribution. For the 300 and 120 $\mu g/ml$ primary IgG samples, the relative errors for $\langle N \rangle$ were 31 and 43%, respectively. For comparison, the $g(0, 0)_j$ values were also averaged across the cell population for each of the samples, and the relative error was determined for each. For the 300 and 120 $\mu g/ml$ primary IgG samples, the relative errors for $\langle g(0, 0) \rangle$ were 35 and 45%, respectively. Thus the biological variation is roughly an order of magnitude greater than the instrumental uncertainty for the ICS measurements of immunolabeled PDGF-β receptors on the surface of human fibroblasts.

As the biological variability was significantly greater than the instrumental uncertainty, we determined cell population averages from the individual occupation numbers ($n_j = g(0, 0)_j^{-1}$), which takes into account the broad nature of the underlying receptor distributions within the AG1523 fibroblast populations. We neglected the much smaller instrumental uncertainty in the calculation of the cell population averages.

An analogous approach showed that the relative error was between 0.2 and 0.5% for individual white noise corrected mean image intensities, whereas a relative error of 20–30% was observed for the cell population distribution of this parameter (data not shown). Consequently, the instrumental uncertainty was also neglected in the calculation of the mean intensity for each cell population.

Cell population means

The cell population averages for the concentration dependence experiment, as calculated from white noise corrected image data, are presented in Fig. 5. In this figure, the population means were not corrected for background fluorescence, so as to allow a direct comparison between the data obtained for the regular samples and that obtained for primary and secondary antibody control samples. A cursory examination of the plots in Fig. 5 reveals that the data follow similar trends: an increase in the value of the dependent variable for intermediate concentrations of the primary label, which eventually plateaus at high concentrations.

The mean population intensity is plotted as a function of primary label concentration in Fig. 5 *A*. As has been pointed out previously, the mean intensity is directly proportional to the total number of fluorophore molecules present on average in the beam area (Petersen, 1986). The mean intensity

TABLE 2 Uncertainty in the estimate of $g(0, 0)$

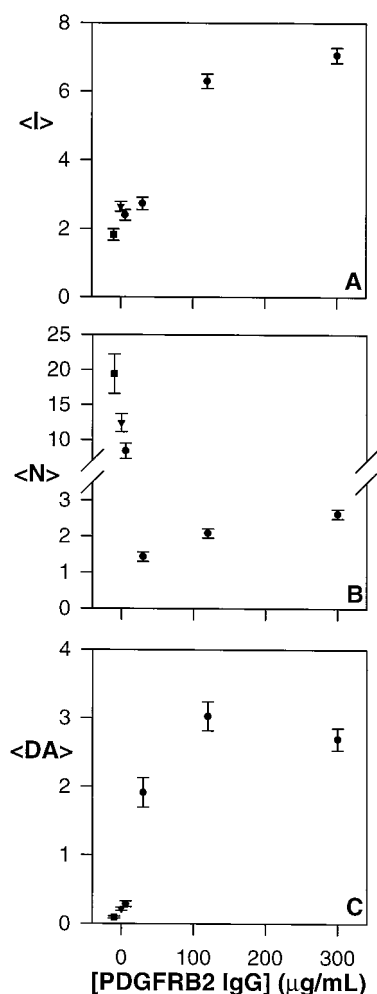| Image	$g(0, 0)$	$\sigma^2_{g(0, 0)}$	$\sigma_{g(0, 0)}$	$\sigma_{g(0, 0)}/g(0, 0)$	Rel. error (%)
1	1.46×10^{-2}	4.7×10^{-7}	6.9×10^{-4}	4.7×10^{-2}	4.7
2	1.84×10^{-2}	6.5×10^{-7}	8.1×10^{-4}	4.4×10^{-2}	4.4
3	7.7×10^{-3}	1.2×10^{-7}	3.4×10^{-4}	4.5×10^{-2}	4.5
4	8.6×10^{-3}	1.6×10^{-7}	4.0×10^{-4}	4.7×10^{-2}	4.7
5	6.0×10^{-3}	7.5×10^{-8}	2.7×10^{-4}	4.5×10^{-2}	4.5

FIGURE 5   Cell population mean results for the concentration dependence ICS measurements of PDGF-β receptors on AG1523 fibroblasts. (*A*) Cell population mean intensity plotted as a function of concentration of the primary antibody label. (*B*) A plot of cell population mean occupation number as a function of primary antibody labeling concentration. (*C*) Population mean degree of aggregation plotted as a function of the labeling concentration of the primary PDGFB2 monoclonal antibody. The primary IgG control sample mean is represented by the square symbol, and the secondary IgG control sample average is depicted by the triangular symbol in all three plots. The primary IgG control mean is plotted with a value of −10 for the abscissa in each figure, simply to facilitate easy visual comparison with the other data. All parameters were calculated from white noise corrected ICS image data. The error bars represent the SEM.

increases concomitantly with the concentration of the primary monoclonal IgG because more of the available cell surface PDGF-β receptor subunits become labeled, and hence detectable. The plateau in mean intensity at high concentrations indicates a saturation level of cell surface receptor subunits, i.e., we have labeled and rendered detectable the cell surface receptor population.

Fig. 5 *B* presents the population mean occupation number as a function of primary antibody concentration. Whereas the intensity reflects the total number of labeled subunits, ⟨*N*⟩ depends on the average number of spatially independent labeled receptor clusters per beam area. The very high mean

occupation numbers seen for the control samples (*square* and *triangular data symbols* in Fig. 5 *B* for the primary and secondary IgG controls, respectively) reflect the small relative fluctuations in the background fluorescence. The small relative fluctuations of the background are manifested in the autocorrelation analysis as a large number of low-intensity particles resulting in large ⟨*N*⟩ (and low intensities) for the control samples. The 6 μg/ml sample also shows a high occupation number, which demonstrates that few receptor subunits (and hence receptor clusters) are labeled at this low concentration, and we mainly see background levels. However, at higher concentrations of the primary label, we begin to detect the underlying receptor population as the subunits within the clusters become specifically labeled, making the aggregates bright relative to the background. A similar "binding" type curve with a plateau is seen for the ⟨*N*⟩ parameter at intermediate and high concentrations of the primary label, which provides evidence that we are detecting all receptor aggregates at the cell surface as their component subunits become saturated with antibody label.

In Fig. 5 *C* we present a plot of a parameter referred to as the "degree of aggregation." In an earlier work, one of the authors demonstrated that the product of the autocorrelation function amplitude and the average intensity was a function of the mean and variance of the distribution of aggregate size and did not depend on the total number of subunits in the observation volume (Petersen, 1986). The degree of aggregation that we present is essentially the same parameter, but calculated for the cell population. As such, this parameter reflects the aggregation state of the detected fluorophore molecules and increases concomitantly with greater clustering of the fluorophore. As for the mean intensity and occupation number, the average degree of aggregation also increases as a function of concentration of the primary label until it reaches a saturation level at high labeling concentrations. These data are also compatible with the previously discussed model of labeling and detection of greater numbers of receptor subunits within clusters until a saturation level is reached. A close examination of Fig. 5 *C* reveals that there is a significant difference between the degree of aggregation of the secondary antibody control sample (*triangular symbol*) and the high concentration samples. Although these data have not been corrected for fluorescence background, this large difference in the degree of aggregation strongly suggests that there is a difference in aggregation state between the nonspecifically bound fluorophore detected in the control sample and the mainly specifically bound fluorophore detected in the high-concentration samples. These data imply that the underlying PDGF-β receptors, which are labeled by the fluorophore-conjugated antibody molecules (indirectly via the monoclonal IgG intermediary), are preaggregated on the surface of human AG1523 fibroblasts.

The cell population means for the 300 μg/ml sample and the 2° IgG control sample were corrected for fluorescence background in the manner outlined in Materials and Methods and explained in the Theory section. Fluorescence back-

ground correction of the 300 μg/ml sample data using the 2° IgG control data provides estimates of population means for the specifically bound fluorophore at saturation binding levels. Likewise, autofluorescence background correction of the 2° IgG control means via the 1° IgG control data yields estimates of the population means for the nonspecifically bound fluorophore. Table 3 presents the background-corrected cell population means estimated for the specifically bound fluorophore at saturation level and for the nonspecifically bound fluorophore. The uncertainties are reported as standard errors of the mean (SEMs) and were derived via propagation of errors analysis of each background correction calculation. A comparison of the mean degrees of aggregation for the specifically and nonspecifically bound fluorophores in Table 3 shows that the former is just over eight times the value of the latter. These background-corrected results provide direct evidence that the PDGF-β receptors are preclustered, as the specific fluorophore is more highly aggregated than the nonspecific fluorophore.

In this experiment, the 2° IgG was an Fab-specific goat anti-mouse antibody. If we assume that two 2° IgG molecules bind to the two Fab portions of each 1° mouse monoclonal antibody, we arrive at an estimate of two fluorophore-conjugated antibodies per PDGF-β receptor (assuming that one monoclonal IgG binds per receptor). Furthermore, if we assume that most of the nonspecific fluorescence is due to individual 2° IgG molecules binding nonspecifically at the cell surface, we can estimate that the PDGF-β are preaggregated as tetramers under these experimental conditions. This assumption is based on the expectation that the binding specificity of the polyclonal 2° antibodies will be less than that of the monoclonal 1° IgG used in this study. We note that analogous results were obtained for an independent concentration dependence ICS experiment using an Fc-specific FITC-conjugated 2° IgG (Wiseman, 1995). An analysis of the background-corrected data from the separate FITC experiment showed that the PDGF-β receptors were preaggregated as trimers or tetramers on average under identical experimental conditions. The interpretation of these independent results was predicated on the assumption that *one Fc-specific* 2° IgG bound per 1° monoclonal antibody (i.e., one per receptor subunit) in the FITC experiment.

We examine the other population parameters presented in Table 3 on the basis of the theoretical framework introduced by Petersen for interpretation of autocorrelation results for a system with a distribution of aggregates of various sizes (Petersen, 1986). Following this earlier theoretical model,

the cell population mean parameters may be formulated in the following ways:

$$\langle I \rangle = c' \langle N_s \rangle \tag{44}$$

$$\langle N_c \rangle = \langle N_s \rangle \left\{ \frac{\mu}{\mu^2 + \sigma^2} \right\} \tag{45}$$

$$\langle DA \rangle = c' \left\{ \frac{\mu^2 + \sigma^2}{\mu} \right\} \tag{46}$$

where $\langle N_s \rangle$ is the mean number of independent fluorescent subunits (i.e., fluorophore-conjugated 2° IgG molecules) per beam area, μ is the mean number of fluorescent subunits per aggregate, σ^2 is the variance of the aggregate size distribution, and c' is an optical constant that depends on incident illumination intensity and the spectroscopic properties of the fluorophore and optical system. As the number of PDGF-β subunits per aggregate was quite small for this system, and the subunit distribution is a discrete function, we made the assumption that the number of PDGF-β subunits per aggregate, as well as the directly proportional distribution of 2° IgG per aggregate, obeys Poisson statistics. In this case, the variance of the distribution equals the mean, and Eq. 45 and 46 may be simplified. Furthermore, the $\langle DA \rangle$ for the nonspecific fluorophore provides an estimate of the optical constant if our assumption of unitary binding of most of the nonspecific fluorophore (with negligible variance) is valid (see Eq. 46). Using this value for c' and Eq. 44, it is possible to estimate the mean number of subunits per beam area ($\langle N_s \rangle$). The mean number of subunits per aggregate (μ) can be determined from Eq. 45 or 46, and the *true* receptor cluster occupation number is the ratio $\langle N_s \rangle / \mu$. Table 4 summarizes these results for specifically and nonspecifically bound fluorophores as well as the corresponding values for the PDGF-β receptors to which the 2° IgG molecules were indirectly bound. The reported uncertainties are SEM determined via propagation of errors analysis of the calculations for the derived quantities. The mean cluster density, $\langle \rho_c \rangle$, is also presented in Table 4. Calculation of $\langle \rho_c \rangle$ simply involves converting the true occupation number to an aggregate density per unit area by using the reciprocal beam area as a conversion factor (i.e., $[\pi \langle \omega \rangle^2]^{-1}$, where $\langle \omega \rangle$ is the mean e^{-2} beam radius determined by

TABLE 3 Fluorescence background-corrected cell population means

2° IgG	$\langle I \rangle$	$\langle N \rangle$	$\langle DA \rangle$
Specific	4.4 ± 0.3	1.1 ± 0.1	4.2 ± 0.4
Nonspecific	0.8 ± 0.2	1.7 ± 0.6	0.5 ± 0.2

Uncertainties are SEM.

TABLE 4 Summary of results for AG1523 fibroblasts

	$\langle N_s \rangle$	μ	$\langle N_s \rangle / \mu$	$\langle \rho_c \rangle$ (μm^{-2})
Nonspecific 2° IgG	1.7 ± 0.6	1 ± 0*	1.7 ± 0.6	3.3 ± 1.2
Specific 2° IgG	9.2 ± 4.1	7.8 ± 3.9	1.2 ± 0.8	2.3 ± 1.5
PDGF-β receptors	4.6 ± 2.0	3.9 ± 2.0	1.2 ± 0.8	2.3 ± 1.5

Uncertainties are SEM.
*By assumption.

averaging the best fit beam radii from the 300 and 120 μg/ml samples).

The data presented in Table 4 demonstrate that the PDGF-β receptors are found to be preclustered as tetramers with an average of 2.3 aggregates μm^{-2} on the surface of AG1523 fibroblasts immunolabeled at 4°C. The wide variation in the fluorescent spot intensities observed within the images (see Fig. 1 *B*) strongly suggests that there is a distribution of aggregate size on the surface of the fibroblasts. As first-order autocorrelation analysis was used in this study, the ICS results presented represent the mean aggregation state for this cellular distribution of PDGF-β cluster size. If we consider both the relatively small average aggregate size measured (tetramer) and the wide dispersion in the spot intensities observed, it is probable that the less intense spots in the images may be attributed to actual PDGF-β monomeric subunits on the cell surface (or in some cases nonspecifically bound fluorophore). Detection and quantification of receptor distributions approaching the monomeric level on normal cells represent a significant experimental achievement and test of the ICS technique.

An implicit assumption in these experiments is that the primary and secondary antibodies do not cause clustering of the PDGF-β receptors at 4°C. This assumption is supported by our earlier ICS time series measurements on PDGF-β receptor distributions on the surface of living AG1523 fibroblasts (Wiseman et al., 1997). In this study, no change in the aggregation state of receptors labeled with primary and secondary antibodies was detected as a function of time for cells maintained at 4°C. However, rapid clustering of the receptors was measured once the cells were warmed to 37°C. In light of the earlier results, we believe that our current study provides strong evidence for the existence of preformed tetramers.

By measuring the mean surface area of the AG1523 cells and using the data derived from ICS measurements, it is possible to obtain an estimate of the total number of PDGF-β receptors on the surface of the fibroblasts. To facilitate this, we performed surface area measurements on immunolabeled AG1523 fibroblasts from two separate samples, using the Biorad MRC600 CLSM, and obtained a mean projected surface area of 5400 $\pm$ 500 μm^2 (SEM, $N =$ 45 cells). Optical sectioning experiments using the CLSM indicated that the ICS measurements were detecting labeled receptors on the upper membrane of the cell but not the receptors on the bottom membrane, which were believed to be inaccessible to the antibody molecules used for labeling (Wiseman, 1995). Thus, for cells with an average total surface area (top and bottom) of 10,800 μm^2, which express an average of 2.3 tetramers per unit area of membrane, we estimate ~100,000 surface PDGF-β receptor subunits. An earlier competitive binding study of PDGF receptor expression in various cell types reported an average expression level of 150,000 PDGF-β subunits for the AG1523 fibroblast cell line, which compares favorably with our ICS measurements (Seifert et al., 1989). This comparison suggests that the ICS measurements presented in this work are

accurate and do represent quantification of the actual PDGF-β receptor distributions on the surface of the AG1523 fibroblasts.

These results provoke questions about the nature of the PDGF-β receptor aggregates, as the ICS experiments reported do not provide information about the underlying membrane domain or mechanism governing the clustering. There are several possible explanations for the nature of the aggregates. The receptors may be preaggregated in clathrin-coated pits in association with the adaptor protein AP-2. It should be noted that the PDGF-β receptors are down-regulated after growth factor ligand binding via the coated-pit-mediated endocytotic pathway (Rosenfeld et al., 1984). However, the small size of the receptor clusters detected mitigates against this possibility, as higher levels of aggregation are generally observed for receptors clustered in coated pits. Moreover, when the fibroblast samples were warmed to 37°C after labeling, significantly higher levels of aggregation were detected via ICS (Wiseman, 1995). As the monoclonal antibody used in this study has been shown to induce down-regulation of the receptors at 37°C, the increase in aggregation detected is consistent with a recruitment of the smaller clusters into larger aggregates in coated pit regions of the membrane.

A second possibility is that the PDGF receptors are preaggregated in caveolae within the membrane. A recent study introduced evidence which suggested that caveolae were the loci of PDGF-initiated signal transduction and were the primary location of the majority of PDGF receptors in the membrane (Liu et al., 1996).

It is also possible that interactions between the cytoplasmic domain of the PDGF-β receptors and the underlying membrane-associated cytoskeleton may be responsible for maintaining the receptors in an aggregated state. There has been a recent accumulation of evidence showing that cell surface receptors and other integral membrane proteins are confined in membrane domains demarcated by the underlying cytoskeleton (Kusumi et al., 1993; Sako and Kusumi, 1994; Kusumi and Sako, 1996). Such interactions may also play a role in regulating the aggregation state of receptors for growth factors like PDGF.

The demonstration that PDGF-β receptors are preaggregated on the surface of human dermal fibroblasts is a significant biological result, as it contradicts one of the basic tenets of the ligand-induced dimerization model. A fundamental assumption of this model is that receptor dimerization (or oligomerization) occurs only after binding of growth factor ligand to uniformly dispersed receptor monomers. The data presented here complement our earlier study involving ICS measurements on living AG1523 fibroblasts at 4°C and 37°C (Wiseman et al., 1997). In the earlier work, we obtained qualitative evidence that the PDGF-β receptors were preaggregated on the surface of AG1523 fibroblasts, but were unable to quantify the aggregation state as we have in the present work. We also demonstrated that treatment of the cells with the growth factor ligand PDGF-BB caused no detectable change in the aggregation state of the receptors at

both temperatures (Wiseman et al., 1997). One interpretation of this observation is that treatment with growth factor has no effect on the aggregation state of receptors that are already clustered. The results presented in the current work demonstrate that the receptors are indeed preaggregated and that an average cluster contains four β-subunits.

The ICS results presented raise questions about the validity of the widely accepted ligand-induced dimerization model and provide support for an alternative model involving signal transduction by a ligand-induced conformational change in preaggregated PDGF-β receptors (the various models are discussed in Williams, 1989). As was noted in the Introduction, much of the evidence supporting the ligand-induced dimerization model was obtained using techniques that entail perturbation of the cells and measurements of receptor aggregation in completely nonphysiological environments. The major advantage of the ICS technique is that it permits quantitative assessment of receptor aggregation state on minimally perturbed cells under physiologically relevant measuring conditions. It is relevant to note that recent studies of oligomerization of epidermal growth factor (EGF) receptors in viable A431 cells using FRET techniques have provided evidence of preclustering of the active high-affinity receptors in the absence of EGF (Gadella and Jovin, 1995). Gadella and Jovin proposed an alternative model for signal transduction involving rotational conformational changes in preexisting EGF dimers after binding of its growth factor ligand. However, as FRET techniques do not yield information on the actual size of the clusters, Gadella and Jovin assumed that the EGF oligomers were preexisting dimers. An earlier study using scanning FCS provided evidence that the EGF receptors were preclustered as oligomers containing ~130 subunits (St-Pierre and Petersen, 1992).

The ICS measurements and background analysis/correction method outlined in this work represent a significant advance, as they involve the application of fluorescence correlation-type methods to the measurement of receptor aggregation in an intact cellular milieu in the presence of background fluorescence for a nontransformed cell line. The AG1523 is of normal phenotype and does not overexpress PDGF-β receptors. Consequently, the number of receptors per unit area on the cell surface is quite low, which makes detection and quantification difficult, especially with omnipresent cellular autofluorescence. However, the combination of the sensitivity of immunofluorescence CLSM imaging with photon counting detection, coupled with autocorrelation analysis and background correction, allowed us to achieve detection of very low levels of receptors.

It is possible to improve on the basic ICS measurement: utilization of two-photon excitation or implementation of two-color fluorescence cross-correlation spectroscopy could further improve the sensitivity and detection limits (Berland et al., 1995, 1996; Srivastava and Petersen, 1996; Schwille et al., 1997). Application of high-order autocorrelation or moment analysis may also permit complete characterization of the aggregate size distribution (Palmer and Thompson,

1989; Qian and Elson, 1990). However, as shown in the present work, careful implementation of the ICS method allows characterization of receptor oligomerization in native cell membranes. As such, this work represents a significant and seminal application of the ICS technique to cell surface aggregation measurements.

REFERENCES

Berland, K. M., P. T. C. So, Y. Chen, W. W. Mantulin, and E. Gratton. 1996. Scanning two-photon fluctuation correlation spectroscopy: particle counting measurements for detection of molecular aggregation. *Biophys. J.* 71:410–420.

Berland, K. M., P. T. C. So, and E. Gratton. 1995. Two-photon fluorescence correlation spectroscopy: method and application to the intracellular environment. *Biophys. J.* 68:694–701.

Carraway, K. L. III, and R. A. Cerione. 1991. Comparison of epidermal growth factor (EGF) receptor-receptor interactions in intact A431 cells and isolated plasma membranes. Large scale receptor micro-aggregation is not detected during EGF-stimulated early events. *J. Biol. Chem.* 266:8899–8906.

Gadella, T. W. Jr., and T. M. Jovin. 1995. Oligomerization of epidermal growth factor receptors on A431 cells studied by time-resolved fluorescence imaging microscopy. A stereochemical model for tyrosine kinase receptor activation. *J. Cell Biol.* 129:1543–1558.

Ghosh, R. N., and W. W. Webb. 1994. Automated detection and tracking of individual and clustered cell surface low density lipoprotein receptor molecules. *Biophys. J.* 66:1301–1318.

Haigler, H., J. F. Ash, S. J. Singer, and S. Cohen. 1978. Visualization by fluorescence of the binding and internalization of epidermal growth factor in human carcinoma cells A-431. *Proc. Natl. Acad. Sci. USA.* 75:3317–3321.

Heldin, C.-H. 1995. Dimerization of cell surface receptors in signal transduction. *Cell.* 80:213–223.

Huang, Z., and N. L. Thompson. 1996. Imaging fluorescence correlation spectroscopy: nonuniform IgE distributions on planar membranes. *Biophys. J.* 70:2001–2007.

Icenogle, R. D., and E. L. Elson. 1983. Fluorescence correlation spectroscopy and photobleaching recovery of multiple binding reactions. I. Theory and FCS measurements. *Biopolymers.* 22:1919–1948.

Koppel, D. E. 1974. Statistical accuracy in fluorescence correlation spectroscopy. *Phys. Rev. A.* 10:1938–1945.

Koppel, D. E., F. Morgan, A. E. Cowan, and J. H. Carson. 1994. Scanning concentration correlation spectroscopy using the confocal laser microscope. *Biophys. J.* 66:502–507.

Kubitscheck, U., M. Kircheis, S. R. Schweitzer, W. Dreybrodt, T. M. Jovin, and I. Pecht. 1991. Fluorescence resonance energy transfer on single living cells. *Biophys. J.* 60:307–318.

Kubitscheck, U., S. R. Schweitzer, D. J. Arndt-Jovin, T. M. Jovin, and I. Pecht. 1993. Distribution of type I Fc epsilon-receptors on the surface of mast cells probed by fluorescence resonance energy transfer. *Biophys. J.* 64:110–120.

Kusumi, A., and Y. Sako. 1996. Cell surface organization by the membrane skeleton. *Curr. Opin. Cell Biol.* 8:566–574.

Kusumi, A., Y. Sako, and M. Yamamoto. 1993. Confined lateral diffusion of membrane receptors as studied by single particle tracking (nanovid microscopy). Effects of calcium-induced differentiation in cultured epithelial cells. *Biophys. J.* 65:2021–2040.

Lemmon, M. A., and J. Schlessinger. 1994. Regulation of signal transduction and signal diversity by receptor oligomerization. *Trends Biol. Sci.* 19:459–463.

Liu, P., Y. Ying, Y.-G. Ko, and R. G. W. Anderson. 1996. Localization of platelet-derived growth factor-stimulated phosphorylation cascade to caveolae. *J. Biol. Chem.* 271:10299–10303.

Metzger, H. 1992. Transmembrane signaling: the joy of aggregation. *J. Immunol.* 149:1477–1487.

Meyer, T., and H. Schindler. 1988. Particle counting by fluorescence correlation spectroscopy: simultaneous measurement of aggregation and diffusion of molecules in solution and in membranes. *Biophys. J.* 54:983–993.

Morrison, I. E. G., C. M. Anderson, G. N. Georgiou, G. V. W. Stevenson, and R. J. Cherry. 1994. Analysis of receptor clustering on cell surface by imaging fluorescent particles. *Biophys. J.* 67:1280–1290.

Palmer, A. G., III, and N. L. Thompson. 1989. Fluorescence correlation spectroscopy for detecting submicroscopic clusters of fluorescent molecules in membranes. *Chem. Phys. Lipids.* 50:253–270.

Pawley, J. 1995. Fundamental limits in confocal microscopy. *In* Handbook of Biological Confocal Microscopy, 2nd Ed. J. B. Pawley, editor. Plenum Press, New York.

Petersen, N. O. 1986. Scanning fluorescence correlation spectroscopy. I. Theory and simulation of aggregation measurements. *Biophys. J.* 49:809–815.

Petersen, N. O., P. L. Höddelius, P. W. Wiseman, O. Seger, and K.-E. Magnusson. 1993. Quantitation of membrane receptor distributions by image correlation spectroscopy: concept and application. *Biophys. J.* 65:1135–1146.

Qian, H. 1990. On the statistics of fluorescence correlation spectroscopy. *Biophys. Chem.* 38:49–57.

Qian, H., and E. L. Elson. 1990. Distribution of molecular aggregation by analysis of fluctuation moments. *Proc. Natl. Acad. Sci. USA.* 87:5479–5483.

Rönnstrand, L., L. Terracio, L. Claesson-Welsh, C. H. Heldin, and K. Rubin. 1988. Characterization of two monoclonal antibodies reactive with external domain of the platelet-derived growth factor receptor. *J. Biol. Chem.* 263:10429–10435.

Rosenfeld, M. E., D. F. Bowen-Pope, and R. Ross. 1984. Platelet-derived growth factor: morphologic and biochemical studies of binding, internalization, and degradation. *J. Cell. Physiol.* 121:263–274.

Sako, Y., and A. Kusumi. 1994. Compartmentalized structure of the plasma membrane for lateral diffusion of receptors as revealed by nanometer-level motion analysis. *J. Cell Biol.* 125:1251–1264.

Schlessinger, J., Y. Shechter, M. C. Willingham, and I. Pastan. 1978. Direct visualization of binding, aggregation, and internalization of insulin and epidermal growth factor on living fibroblastic cells. *Proc. Natl. Acad. Sci. USA.* 75:2659–2663.

Schwille, P., F. J. Meyer-Almes, and R. Rigler. 1997. Dual-color fluorescence cross-correlation spectroscopy for multicomponent diffusional analysis in solution. *Biophys. J.* 72:1878–1886.

Seifert, R. A., C. E. Hart, P. E. Phillips, J. W. Forstrom, R. Ross, M. J. Murray, D. F. Bowen-Pope. 1989. Two different subunits associate to create isoform-specific platelet-derived growth factor receptors. *J. Biol. Chem.* 264:8771–8778.

Srivastava, M., and N. O. Petersen. 1996. Image cross-correlation spectroscopy: a new experimental biophysical approach to measurement of slow diffusion of fluorescent molecules. *Methods Cell Sci.* 18:47–54.

St-Pierre, P. R., and N. O. Petersen. 1992. Average density and size of microclusters of epidermal growth factor receptors on A431 cells. *Biochemistry.* 31:2459–2463.

Thompson, N. L. 1991. Fluorescence correlation spectroscopy. *In* Topics in Fluorescence Spectroscopy, Vol. 1. J. R. Lakowicz, editor. Plenum Press, New York.

Thompson, N. L., and D. Axelrod. 1983. Immunoglobulin surface-binding kinetics studied by total internal reflection with fluorescence correlation spectroscopy. *Biophys. J.* 43:103–114.

Ullrich, A., and J. Schlessinger. 1990. Signal transduction by receptors with tyrosine kinase activity. *Cell.* 61:203–212.

Van Belzen, N., P. J. Rijken, W. J. Hage, S. W. de Laat, A. J. Verkleij, and J. Boonstra. 1988. Direct visualization and quantitative analysis of epidermal growth factor-induced receptor clustering. *J. Cell. Physiol.* 134:413–420.

Wang, M. D., and D. Axelrod. 1994. Microclustering patterns of acetylcholine receptors on myotubes studies by spatial fluorescence autocorrelation. *Bioimaging.* 2:22–35.

Williams, L. T. 1989. Signal transduction by the platelet-derived growth factor receptor. *Science.* 243:1564–1570.

Wiseman, P. W. 1995. Image correlation spectroscopy: development and application to studies of PDGF receptor distributions. Ph.D. thesis. The University of Western Ontario, London, ON.

Wiseman, P. W., P. Höddelius, N. O. Petersen, and K. Magnusson. 1997. Aggregation of PDGF-β receptors in human skin fibroblasts: characterization by image correlation spectroscopy (ICS). *FEBS Lett.* 401:43–48.

Young, R. M., J. K. Arnette, D. A. Roess, and B. G. Barisas. 1994. Quantitation of fluorescence energy transfer between cell surface proteins via fluorescence donor photobleaching kinetics. *Biophys. J.* 67:881–888.